

# $\text{Li}_6\text{SiO}_4\text{Cl}_2$ : A Hexagonal Argyrodite Based on Antiperovskite Layer Stacking

Alexandra Morscher, Matthew S. Dyer, Benjamin B. Duff, Guopeng Han, Jacinthe Gamon, Luke M. Daniels, Yun Dang, T. Wesley Surta, Craig M. Robertson, Frédéric Blanc, John B. Claridge, and Matthew J. Rosseinsky\*



Cite This: *Chem. Mater.* 2021, 33, 2206–2217



Read Online

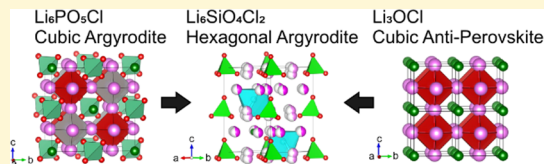
ACCESS |

Metrics & More

Article Recommendations

Supporting Information

**ABSTRACT:** A hexagonal analogue,  $\text{Li}_6\text{SiO}_4\text{Cl}_2$ , of the cubic lithium argyrodite family of solid electrolytes is isolated by a computation–experiment approach. We show that the argyrodite structure is equivalent to the cubic antiperovskite solid electrolyte structure through anion site and vacancy ordering within a cubic stacking of two close-packed layers. Construction of models that assemble these layers with the combination of hexagonal and cubic stacking motifs, both well known in the large family of perovskite structural variants, followed by energy minimization identifies  $\text{Li}_6\text{SiO}_4\text{Cl}_2$  as a stable candidate composition. Synthesis and structure determination demonstrate that the material adopts the predicted lithium site-ordered structure with a low lithium conductivity of  $\sim 10^{-10} \text{ S cm}^{-1}$  at room temperature and the predicted hexagonal argyrodite structure above an order–disorder transition at  $469.3(1) \text{ K}$ . This transition establishes dynamic Li site disorder analogous to that of cubic argyrodite solid electrolytes in hexagonal argyrodite  $\text{Li}_6\text{SiO}_4\text{Cl}_2$  and increases Li-ion mobility observed via NMR and AC impedance spectroscopy. The compositional flexibility of both argyrodite and perovskite alongside this newly established structural connection, which enables the use of hexagonal and cubic stacking motifs, identifies a wealth of unexplored chemistry significant to the field of solid electrolytes.



## 1. INTRODUCTION

Compounds related to the mineral argyrodite ( $\text{Ag}_8\text{GeS}_6$ ) have been the focus of considerable interest for over half a century. The argyrodite family is compositionally flexible, with the general formula  $\text{A}_{(12-n-y)/m}\text{L}_{6-y}^{n+}\text{X}_{6-y}^{2-}\text{Y}_y^-$  ( $\text{A} = \text{Ag}^+, \text{Cu}^+, \text{Cd}^{2+}$ , etc.;  $\text{L} = \text{Ga}^{3+}, \text{Si}^{4+}, \text{Ge}^{4+}, \text{P}^{5+}$ , etc.;  $\text{X} = \text{S}^{2-}, \text{Se}^{2-}, \text{Te}^{2-}$ ;  $\text{Y} = \text{Cl}^-, \text{Br}^-, \text{I}^-$ ),<sup>1</sup> where the A cation content can vary from 3.25 to 9 to maintain charge neutrality. This family of compounds contains examples of fast  $\text{Ag}^+$  and  $\text{Cu}^+$  ion conductors (e.g.,  $\text{Cu}_6\text{PS}_5\text{Cl}$ <sup>1</sup> and  $\text{Ag}_7\text{NbS}_6$ <sup>2</sup>) as well as materials interesting for their nonlinear optical properties (e.g.,  $\text{Cd}_{3.25}\text{PS}_{5.5}\text{I}_{0.5}$ <sup>1</sup>) and thermoelectric properties (e.g.,  $\text{Ag}_8\text{SnSe}_6$ <sup>3</sup>).

The reported crystal structures of argyrodites are related to the high-temperature  $F\bar{4}3m$  cubic polymorph of  $\text{Ag}_8\text{GeS}_6$ , where A cations often demonstrate an extended dynamic disorder. Static ordering of cations at low temperatures, along with the corresponding structural displacements, can lead to low-temperature polymorphs with lower symmetry.<sup>4,5</sup> This dynamic disorder in higher-symmetry polymorphs has led to extensive investigations of argyrodites as potential solid-state electrolytes in all solid-state lithium-ion batteries (ASSBs).<sup>6,7</sup> In the lithium-containing argyrodites, the introduction of a halide anion transforms the room-temperature orthorhombic polymorph ( $\text{Li}_7\text{PCh}_6$  ( $\text{Ch} = \text{S}, \text{Se}$ ): space group  $Pna2_1$ ) into cubic symmetry ( $\text{Li}_6\text{PCh}_5\text{X}$  ( $\text{X} = \text{Cl}, \text{Br}, \text{I}$ ): space group  $F\bar{4}3m$ ), while charge compensation occurs via reduction of the lithium content. The latter cubic phase exhibits an order–

disorder phase transition from static order (LT cubic phase) to an extended dynamic disorder (HT cubic phase), with delocalization of the lithium distribution.<sup>8</sup> In cubic oxide analogues such as  $\text{Li}_6\text{PO}_5\text{Br}$ , this phase transition does not occur, and lithium localization within the  $F\bar{4}3m$  structure is maintained over a wide temperature range (173–873 K).<sup>9</sup> In the ordered  $F\bar{4}3m$  structure of  $\text{Li}_6\text{PO}_5\text{Br}$ , lithium ions fully occupy a single crystallographic  $24g$  position. In the dynamically disordered HT  $F\bar{4}3m$  structure of the lithium sulfide argyrodites, the additional available lithium sites (Wyckoff position  $48h$ ) and extended diffusion of  $\text{Li}^+$  are linked to a dramatic increase in ionic conductivity by six orders of magnitude.<sup>10,11</sup> The most highly conducting Li-containing argyrodites are based on mixed sulfide–halide compositions, e.g.,  $\text{Li}_6\text{PS}_5\text{Br}$ <sup>6</sup> and  $\text{Li}_{6.35}\text{P}_{0.65}\text{Si}_{0.35}\text{S}_5\text{Br}$ , in which  $\text{Li}^+$  is delocalized across  $48h$  and  $24g$  positions.<sup>12</sup>

The high-temperature  $F\bar{4}3m$  argyrodite structure has previously been described in terms of tetrahedral close-packing<sup>1</sup> or as localized pseudo-octahedral cages of A cations surrounding one anion and separated by the other anions.<sup>10,11</sup>

Received: January 15, 2021

Revised: February 15, 2021

Published: March 2, 2021



In this work, we establish a new relationship between the structures of argyrodites and those of cubic antiperovskites, which are themselves good conductors of lithium ions (i.e.,  $\text{Li}_3\text{OCl}_{1-x}\text{Br}_x$ ).<sup>13</sup> We extend this relationship, which provides a framework for designing lithium-ion conductors, from cubic to hexagonal antiperovskites and thus propose the lithium hexagonal argyrodite family, computationally identifying several new compositional targets within this family.  $\text{Li}_6\text{SiO}_4\text{Cl}_2$  is then successfully synthesized following these predictions based on mixed cubic and hexagonal stacking and shows analogous dynamical cation site disorder to cubic argyrodites, which is required for Li transport.

## 2. EXPERIMENTAL PROCEDURE

**2.1. Computational Methods.** Periodic plane-wave-based density functional theory (DFT) calculations were performed using the VASP code (version 5.4.4).<sup>14</sup> All calculations were performed with the projector-augmented wave method,<sup>15</sup> a plane-wave cutoff energy of 700 eV, and a  $k$ -point spacing of  $0.15 \text{ \AA}^{-1}$ . Geometry optimization of both atomic positions and unit cell parameters was terminated once all forces fell below  $0.001 \text{ eV \AA}^{-1}$ . The PBE functional<sup>16</sup> was used to calculate relative energies and mechanical properties, and the PBEsol functional<sup>17</sup> was used for direct comparison between computational and experimental crystal structures. The convex hull of energies for all reported phases in the  $\text{Li}-\text{Si}-\text{O}-\text{Cl}-\text{Br}$  and  $\text{Li}-\text{Si}-\text{O}-\text{Cl}-\text{I}$  phase fields was calculated using pymatgen.<sup>18</sup> Normal mode calculations were performed using the harmonic approximation, with finite displacements of  $0.01 \text{ \AA}$  and including distortions of the unit cell. This allowed the calculation of elastic constants, including the bulk and shear moduli.<sup>19</sup> For comparison with existing compounds, the elastic constants of  $\text{Li}_3\text{OBr}$  ( $Pm\bar{3}m$  structure)<sup>20</sup> and  $\text{Li}_6\text{PS}_5\text{Br}$  ( $Cc$  structure of  $\text{Li}_6\text{PS}_5\text{I}$ )<sup>21</sup> were computed using the same method.

**2.2. Synthesis.** **2.2.1. Materials.**  $\text{Li}_2\text{CO}_3$  (99.99%),  $\text{SiO}_2$  (silica gel, technical grade, particle size 40–63  $\mu\text{m}$ ), and  $\text{LiCl}$  (>99.0%) were purchased from Sigma-Aldrich.

**2.2.2. Synthesis of  $\text{Li}_4\text{SiO}_4$ .**<sup>22</sup> Precursors were dried overnight at 473 K before weighing.  $\text{Li}_2\text{CO}_3$  (1.2331 g) and  $\text{SiO}_2$  (0.5013 g) were weighed according to the stoichiometric 2:1 ratio. The powders were ground with an agate pestle and mortar for 15 min, placed into an alumina crucible and heated in air to 1073 K at a ramp rate of  $5 \text{ K min}^{-1}$ , held at 1073 K for 12 h, and cooled at a ramp rate of  $5 \text{ K min}^{-1}$ . The resulting product was ground to obtain a fine powder, which was then used as a precursor in the final synthesis step.

**2.2.3. Synthesis of  $\text{Li}_6\text{SiO}_4\text{Cl}_{2-x}\text{Br}_x$ .**  $\text{Li}_4\text{SiO}_4$ ,  $\text{LiCl}$ , and  $\text{LiBr}$  were vacuum-dried overnight (under  $10^{-4}$  mbar) before placing them in an Ar-filled glovebox. All precursors and resulting powders were then handled in an Ar-filled glovebox.  $\text{LiCl}$ ,  $\text{LiBr}$ , and  $\text{Li}_4\text{SiO}_4$  were mixed in the stoichiometric ratio, ground with an agate pestle and mortar for 15 min, and transferred to an alumina crucible. The crucible was placed in a silica tube, which was sealed under vacuum ( $<10^{-4}$  mbar). The tube was heated to 798 K at a ramp rate of  $5 \text{ K min}^{-1}$ , held at 798 K for 12 h, and cooled at a rate of  $5 \text{ K min}^{-1}$ . Once cooled, the silica tube was opened inside the Ar glovebox, and the powder was ground in a pestle and mortar for further characterization.

Single crystals of  $\text{Li}_6\text{SiO}_4\text{Cl}_2$  were grown by mixing  $\text{LiCl}$  and  $\text{Li}_4\text{SiO}_4$  in the stoichiometric ratio, heating the mixture to 883 K at a ramp rate of  $5 \text{ K min}^{-1}$ , annealing it for 3 h, and slow cooling at  $3 \text{ K h}^{-1}$  to room temperature.

**2.3. Powder X-ray Diffraction.** Routine assessment of sample purity was carried out using a Bruker D8 Discover diffractometer with monochromatic Cu radiation ( $\text{K}\alpha_1$ ,  $\lambda = 1.54056 \text{ \AA}$ ) in a Debye Scherrer transmission geometry with sample powders loaded into 0.5 mm borosilicate glass capillaries.

Synchrotron X-ray diffraction (SXRD) was performed at Diamond Light Source U.K., on high-resolution beamline I11,<sup>23</sup> at  $\lambda = 0.826552 \text{ \AA}$ . The pattern was recorded in transmission mode [ $0^\circ < 2\theta < 150^\circ$ ] using a multianalyzer crystal (MAC) detector. The sample was

introduced into a 1.0 mm diameter borosilicate glass capillary. The experiment was performed at room temperature.

Synchrotron variable temperature X-ray diffraction (VT-XRD) was performed in transmission mode using a position-sensitive detector (PSD,  $\lambda = 0.82660 \text{ \AA}$ ) on a sample, which was introduced into a 1.0 mm diameter silica capillary. The experiment was performed in the temperature range of 298–798 K in 25 K steps on heating and then cooled directly to room temperature to assess reversibility.

Rietveld refinements were carried out using TOPAS Academic.<sup>24</sup> Initially, Pawley fits were performed on SXRD data, refining the lattice parameters and the background using a Chebyshev function with 12 parameters. The peak shape was modeled using a pseudo-Voigt function (high-temperature patterns) and a Thomson–Cox function (room-temperature patterns). Refined parameters from final Pawley fits were then used as starting points for Rietveld refinements where the following parameters were refined: (1) scale factor, (2) atomic coordinates, (3) isotropic (Li, Si, O) and anisotropic (Cl) displacement parameters, and (4) atomic occupancies: the occupancies of Cl and O, and Li were refined, while the occupancy of the Si site was set to the nominal value and the Li occupancies were set to ensure charge compensation.

**2.4. Single-Crystal X-ray Diffraction.** A twinned crystal was examined with a Rigaku MicroMax-007 HF X-ray generator equipped with a Mo  $K\alpha$  rotating-anode microfocus source and a Saturn 724+ detector. The data were collected at 100 K. Refinement of the cell parameters, indexing of twin components, and reduction of the data were performed on the obtained diffraction images with the use of the software package CrysAlisPro.<sup>25</sup> The volume ratio of the twin components was about 1:1. The degree of overlap of two components is around 1%. The twin operator is  $92.82^\circ$  rotation around the  $-0.59\ 0.37 -0.72$  reciprocal axis. The detwinned HKLF4 format file was used for structure solution using Olex2.<sup>26</sup> The crystal structure was solved with the intrinsic phasing method provided by the ShelXT<sup>27</sup> structure solution program. Refinements were carried out with the ShelXL<sup>28</sup> refinement package using least-squares minimization.

**2.5. Differential Scanning Calorimetry (DSC).** Heat flux profiles were measured from 15.1 mg of powdered sample in a 40  $\mu\text{L}$  aluminum crucible cold-welded under an Ar atmosphere ( $<0.1 \text{ ppm O}_2, \text{H}_2\text{O}$ ) using a Netzsch DSC 404 F1 differential scanning calorimeter. Data were recorded on heating to 823 K and then cooling to 323 K using heating and cooling rates of  $10 \text{ K min}^{-1}$  under a constant  $50 \text{ mL min}^{-1}$  flow of helium. The transition temperature is the average of the values obtained from both the heating and cooling curves, which were extracted through peak fitting.

**2.6. Alternating current (AC) Impedance Spectroscopy and Direct Current (DC) Polarization.** A pellet of  $\text{Li}_6\text{SiO}_4\text{Cl}_2$  was made by uniaxially pressing  $\sim 30$  mg of material in an 8 mm cylindrical steel die at a pressure of 125 MPa. The pellet was sintered in an evacuated, flame-dried silica tube for 12 h at 848 K. Using this method, a relative density of 84% was achieved.

AC impedance measurements were conducted using an impedance analyzer (Keysight impedance analyzer E4990A). A sputtered gold coating of 300 nm thickness was used as the ion blocking electrodes. Sputtering was achieved under an argon atmosphere using a Q150R sputter coater, and temperature-dependent conductivity measurements were performed under an argon atmosphere over a frequency range of 2 MHz to 20 Hz (with an amplitude of 100 mV). Measurements were performed in the temperature range of 333–575 K in 20 K steps. The ZView2 program<sup>29</sup> was used to fit the impedance spectra with an equivalent circuit.

A pellet of 84% relative density was used for DC potentiostatic polarization measurements. DC polarization data was collected at 300 °C on a Au| $\text{Li}_6\text{SiO}_4\text{Cl}_2$ |Au symmetric cell by applying constant potentials of 0.05, 0.1, 0.5, and 1 V for 7200 s and monitoring the current variation with time. Once a constant current was achieved, the current was recorded and plotted against the applied voltage allowing for the electronic conductivity ( $\sigma_e$ ) to be extracted from the following equation

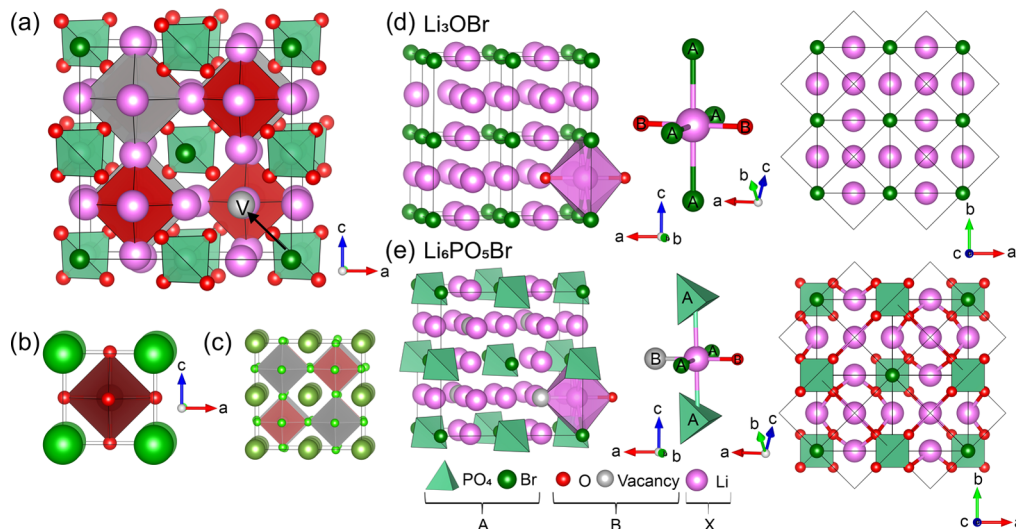


**Figure 1.** (a) Cubic argyrodite structure of  $\text{Li}_6\text{PO}_5\text{Br}$  (Li: pink, P: light green, O: red, Br: dark green, vacant B-site (V): gray; the arrow shows the direction of the P–O bond vector oriented toward the vacant B-site), showing the relationship with (b) the cubic perovskite  $\text{SrTiO}_3$  (Sr: green, Ti: dark red, O: red) and (c) the B-site vacancy-ordered  $\text{K}_2\text{PtCl}_6$  (K: dark green, Pt: red, Cl: light green, vacancies: gray). (d) Cubic antiperovskite structure of  $\text{Li}_3\text{OBr}$ , highlighting the octahedral coordination environment of Li, coordinated by four A-site (Br: dark green) and two B-site (O: red) anions. (e) Compared with  $\text{Li}_3\text{OBr}$ , the cubic argyrodite structure of  $\text{Li}_6\text{PO}_5\text{Br}$  has a reduced Li coordination number defined by four A-site (Br: dark green,  $\text{PO}_4^{3-}$ : polyanion light green) and one B-site anion (O: red) with half of the B-sites vacant (vacancy: gray).

$$\sigma_e = \frac{Il}{UA} \quad (1)$$

where  $U$  refers to the polarization voltage,  $l$  refers to the pellet thickness,  $A$  refers to the Au electrode area, and  $I$  refers to the current.

**2.7. Nuclear Magnetic Resonance (NMR) Spectroscopy.**  $^{29}\text{Si}$  magic-angle spinning (MAS) NMR spectra were recorded with a 4 mm HXY MAS probe in double resonance mode on a Bruker 9.4 T Avance III HD spectrometer.  $^{29}\text{Si}$  NMR data was obtained using a pulse length of 5  $\mu\text{s}$  at a radio frequency (rf) amplitude of 50 kHz and at an MAS rate of  $\nu_r = 10$  kHz. The sample was packed into a rotor in an Ar-filled glovebox to eliminate exposure to air and moisture.  $^{29}\text{Si}$  chemical shifts were externally referenced to the lowest-frequency signal of octakis(trimethylsiloxy)silsesquioxane at  $-109$  ppm,<sup>30</sup> relative to tetramethylsilane primary reference at 0.0 ppm.

Variable temperature  $^7\text{Li}$  NMR experiments were recorded with a 4 mm HX High-Temperature MAS Probe on a 9.4 T Bruker Avance III HD spectrometer under static conditions with the X channel tuned to  $^7\text{Li}$  at  $\omega_0/2\pi$  ( $^7\text{Li}$ ) = 156 MHz. The sample was sealed in a glass ampoule, and the spectra were recorded with a pulse length of 1.5  $\mu\text{s}$  at an rf field amplitude of  $\omega_1/2\pi = 83$  kHz and referenced to 10 M LiCl in  $\text{D}_2\text{O}$  at 0 ppm.

The homonuclear dipolar coupling constant between two  $^7\text{Li}$  nuclear spins  $d_{^7\text{Li}^7\text{Li}}$  (in Hz) can be calculated via the following expression

$$d_{^7\text{Li}^7\text{Li}} = -\frac{\mu_0}{8\pi^2} \frac{\hbar\gamma_{^7\text{Li}}^2}{r_{\text{LiLi}}^3} \quad (2)$$

where  $\mu_0$  is the permeability of free space,  $\hbar$  is the reduced Planck's constant,  $\gamma_{^7\text{Li}}$  is the gyromagnetic ratio of  $^7\text{Li}$ , and  $r_{\text{LiLi}}$  is the Li–Li distance.

Temperature calibrations were performed using the chemical shift thermometers  $\text{Pb}(\text{NO}_3)_2$  using  $^{207}\text{Pb}$  NMR<sup>31</sup> and by monitoring the phase transition of  $\text{CuI}$  and  $\text{CuBr}$  using  $^{63}\text{Cu}$  NMR.<sup>32,33</sup> The errors associated with this method were calculated using the isotropic peak line broadening and range from 5 to 20 K.

**2.8. Maximum Entropy Methods (MEM).** Maximum entropy method (MEM) analysis was performed on SXRD and VT-XRD data using the software Jana2006<sup>34</sup> and BayMEM.<sup>35</sup> Rietveld models from Topas were input into Jana2006, which was used to extract  $F_{\text{obs}}$  and generate MEM inputs. BayMEM was used to calculate the electron

density distribution using the  $F_{\text{obs}}$  and the number of electrons in the nominal stoichiometry. Calculations using the number of electrons associated with a 10% Li deficiency were also performed for all models investigated and found to have negligible impact in the resulting electron density distributions. All MEM results were visualized in the VESTA crystal structure visualization software.<sup>36</sup>

### 3. RESULTS AND DISCUSSION

**3.1. Selection of Target Compounds by Structural Analogy between Argyrodite and Perovskite.** We describe the relationship between the argyrodite structure, exemplified by  $\text{Li}_6\text{PO}_5\text{Br}$  (Figure 1a), and the cubic antiperovskite structure. In analogy with perovskites of general formula  $\text{ABX}_3$ ,  $\text{Li}_6\text{PO}_5\text{Br}$  can be written as  $[(\text{PO}_4)_{0.5}\text{Br}_{0.5} \cdot (\text{O}_{0.5}\square_{0.5})\text{Li}_3]$ , where  $\square$  is a vacancy. As such,  $\text{Li}_6\text{PO}_5\text{Br}$  could be considered as an inverse double perovskite. When viewed as a cubic antiperovskite, the lithium ions in  $\text{Li}_6\text{PO}_5\text{Br}$  replace the anion positions in the conventional cubic perovskite (e.g.,  $\text{SrTiO}_3$ ;<sup>37</sup> Figure 1b). The phosphate polyanions and bromide anions replace the larger A-site cations in a rock-salt-ordered fashion. As the cubic perovskite can be represented as a cubic close-packed stacking of  $\text{AX}_3$  layers along [111], here the cubic stacking is an alternation of  $\text{Li}_3\text{Br}$  and  $\text{Li}_3\text{PO}_4$  layers that produces the rock-salt anion ordering. The remaining, isolated oxide anions, then occupy half of the octahedral B-site positions between these layers also in an ordered manner, leaving the other half of the B-sites vacant. The P–O bond vector of each tetrahedral  $\text{PO}_4^{3-}$  anion is directed toward the vacant B-sites, coupling the rock-salt order of the two A-site anions to the anion vacancy defect ordering on the B-site. Rock-salt order of 50% B-site vacancies occurs in the structure of well-known  $\text{K}_2\text{PtCl}_6$ <sup>38</sup> (Figure 1c). When considering these structural similarities between the lithium argyrodites and the lithium antiperovskites, it is evident that the lithium sites in both structures are topologically equivalent. As a result, both structures share the same network of connectivity between lithium sites (Figure 1d,e), suggesting that the underlying mechanism for high ionic conductivity is

common to both material families. The existence of both cubic and hexagonal perovskites associated with the distinct stackings of the  $\text{AX}_3$  layers suggests the existence of hexagonal Li argyrodites that are also based on alternating  $\text{Li}_3\text{Br}$  and  $\text{Li}_3\text{PO}_4$  stackings.

Although closely related in composition to argyrodite, the compound  $\text{Cu}_8\text{GeSe}_6$  has a hexagonal  $P6_3mc$  high-temperature polymorph rather than the cubic  $F\bar{4}3m$  argyrodite structure,<sup>39–41</sup> as do the compounds  $\text{Ag}_5\text{PS}_4\text{I}_2$ <sup>42</sup> and  $\text{Li}_8\text{SiO}_6$ .<sup>43,44</sup> Analysis of these structures shows that they contain similar close-packed layers to those present in the cubic antiperovskite description of the argyrodite family, but that, instead of a  $-c-$  ( $-a-b-c-$ ) close-packed stacking, they are stacked in a  $-h-c-h-c-$  ( $-a-b-a-c-$ ) manner, as would occur in a hexagonal antiperovskite. Different close-packed layer stacking motifs are known within the antiperovskites.<sup>44</sup> The argyrodite/cubic antiperovskite structural relationship suggests that Li-containing materials based on the hexagonal, rather than cubic, antiperovskite stacking of these layers, related to the hexagonal structures of  $\text{Cu}_8\text{GeSe}_6$  and  $\text{Ag}_5\text{PS}_4\text{I}_2$ , would be analogous to the lithium-containing argyrodites, where the number of Li sites and extent of Li ordering among them control ionic conductivity.

Starting from the cubic  $\text{Li}_6\text{PO}_5\text{X}$  ( $\text{X} = \text{Cl}, \text{Br}$ ) argyrodites, the phosphate ( $\text{PO}_4$ )<sup>3-</sup> (P–O bond length: 1.54 Å) was replaced with silicate ( $\text{SiO}_4$ )<sup>4-</sup> (Si–O bond length: 1.65 Å) to increase the A-site cation radius and thus drive a cubic to hexagonal transition through the perovskite tolerance factor ( $r_{\text{P(V)}} = 0.17$  Å,  $r_{\text{Si(IV)}} = 0.26$  Å).<sup>45</sup> The isolated oxide ion was replaced by a halide ion (F, Cl, Br, I) to balance charge. Structures were built with compositions  $\text{Li}_6\text{SiO}_4\text{XX}'$  ( $\text{X}, \text{X}' = \text{F}, \text{Cl}, \text{Br}, \text{I}$ ) with the  $-h-c-h-c-$  ( $-a-b-a-c-$ ) stacking pattern, following  $\text{Cu}_8\text{GeS}_6$ , in the  $P6_3mc$  space group. This affords a hexagonal antiperovskite in which half of the A-sites are occupied with silicate polyanions and half with halide anions. Half of the B-sites are then occupied in an ordered manner by the remaining halide anions, with the vacant B-sites chosen to avoid interactions between the halide anions and the corners of the silicate tetrahedra (Figure 2a).

This is a hexagonal analogue of the  $\text{Li}_6\text{PO}_5\text{Br}$  structure described previously and an inverse analogue of the 4H-hexagonal perovskites (e.g., 4H- $\text{BaMnO}_3$ ,<sup>46</sup> stacking sequence  $-h-c-h-c-$  ( $-a-b-a-c-$ ); Figure 2b). These hexagonal Li argyrodites contain similar close-packed  $\text{AX}_3$  layers to the cubic argyrodites (i.e., alternating  $\text{Li}_3\text{Br}$  and  $\text{Li}_3\text{PO}_4/\text{Li}_3\text{SiO}_4$  layers) but they are stacked in a  $-h-c-h-c-$  ( $-a-b-a-c-$ ) pattern and not a  $-c-$  ( $-a-b-c-$ ) stacking pattern (Figure 2c–h). These compositions were then screened computationally to find the lower-energy structures.

Periodic DFT calculations showed that the composition  $\text{Li}_6\text{SiO}_4\text{ClBr}$  in this  $P6_3mc$  structure was the most stable when compared with a stoichiometric combination of lithium orthosilicate  $\text{Li}_4\text{SiO}_4$  and the relevant binary lithium halides ( $\text{LiCl}$  and  $\text{LiBr}$ ) (Table S1). Through phonon calculations, lower-energy structures than the high-symmetry hexagonal structures were found, arising from the rotation of lithium atoms off the mirror plane of  $P6_3mc$  through activation of displacive  $\Gamma_2$ ,  $\Gamma_3$ ,  $\Gamma_5$ ,  $M_2$ , and  $M_3$  modes (Figure 3b), leading to four potential lower-symmetry polymorphs in space groups  $P31c$ ,  $P6_3$ ,  $Pna2_1$ , and  $Pca2_1$ . The stabilities of all compositions were recomputed in these four lower-symmetry polymorphs, revealing that  $\text{Li}_6\text{SiO}_4\text{Cl}_2$ ,  $\text{Li}_6\text{SiO}_4\text{Br}_2$ ,  $\text{Li}_6\text{SiO}_4\text{ClBr}$ , and

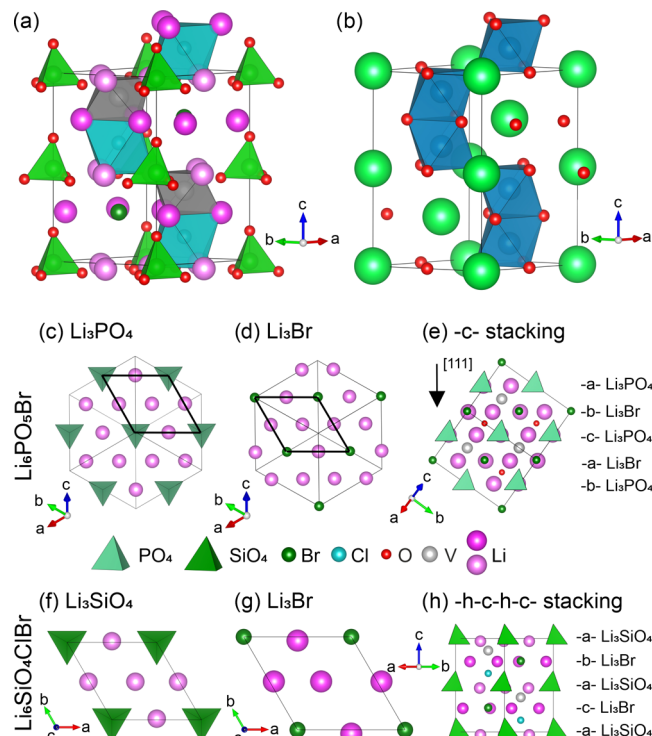


**Figure 2.** (a) DFT-optimized  $P6_3mc$  structure of  $\text{Li}_6\text{SiO}_4\text{ClBr}$  (Li: pink, Si: light green, O: red, Br: dark green, Cl: blue, vacant B-site: gray) is compared to (b) the 4H- $\text{BaMnO}_3$  hexagonal perovskite structure (Ba: green, Mn: blue, O: red). The oxide anions in the conventional hexagonal perovskite are replaced by lithium cations in  $\text{Li}_6\text{SiO}_4\text{ClBr}$ , the A-site barium cations are replaced by an ordered mixture of silicate polyanions and bromide anions, and the B-site manganese cations are replaced by ordered chloride anions and vacancies. In  $\text{Li}_6\text{SiO}_4\text{ClBr}$ , close-packed  $\text{Li}_3\text{Br}$  layers (dark pink lithium) alternate along the  $c$ -direction with close-packed  $\text{Li}_3\text{SiO}_4$  layers (light pink lithium) in an  $-a-b-a-c-$  stacking sequence. Half of the octahedral B-sites between these layers are then occupied by chlorine anions (blue octahedra), leaving half of the B-sites vacant (gray octahedra). (c–h) Comparing close-packed  $\text{AX}_3$  layers in  $\text{Li}_6\text{PO}_5\text{Br}$  cubic argyrodite (viewed along the [111] direction in (c) and (d), and computed  $\text{Li}_6\text{SiO}_4\text{ClBr}$  hexagonal argyrodite viewed along [001] in (f) and (g)): (c)  $\text{Li}_6\text{PO}_5\text{Br}$ :  $\text{Li}_3\text{PO}_4$  layer, (d)  $\text{Li}_6\text{PO}_5\text{Br}$ :  $\text{Li}_3\text{Br}$  layer, and (e)  $\text{Li}_6\text{PO}_5\text{Br}$ : cubic  $(-a-b-c-)$  stacking of close-packed  $\text{Li}_3\text{Br}$  and  $\text{Li}_3\text{PO}_4$  layers. Oxygen atoms (red) and vacancies (gray) occupy octahedral B-sites between the close-packed layers (f)  $\text{Li}_6\text{SiO}_4\text{ClBr}$ :  $\text{Li}_3\text{SiO}_4$  layer, (g)  $\text{Li}_6\text{SiO}_4\text{ClBr}$ :  $\text{Li}_3\text{Br}$  layer, and (h)  $\text{Li}_6\text{SiO}_4\text{ClBr}$ :  $-h-c-h-c-$  ( $-a-b-a-c-$ ) stacking of close-packed  $\text{Li}_3\text{Br}$  and  $\text{Li}_3\text{SiO}_4$  layers. Chlorine atoms (blue) and vacancies (gray) occupy octahedral B-sites between the close-packed layers. For all further figures, all (poly)anions occupying the A-site are drawn in green and all B-site anions are drawn in blue.

$\text{Li}_6\text{SiO}_4\text{Cl}_2$  were predicted to be stable (Figure 3a, Table 1, and Table S1).

These results suggest that a new lithium hexagonal argyrodite family of compounds may be experimentally accessible, with  $\text{Li}_6\text{SiO}_4\text{Cl}_2$  and  $\text{Li}_6\text{SiO}_4\text{ClBr}$  (with the larger Br ordered on the A-site) predicted to be the most stable and chosen as targets for experimental synthesis.

DFT calculations of the elastic constants of  $\text{Li}_6\text{SiO}_4\text{Cl}_2$  in the  $Pna2_1$  structure result in a computed bulk modulus,  $B_{\text{DFT}}$ , of 53 GPa and a computed shear modulus,  $G_{\text{DFT}}$ , of 31 GPa. This material is considerably softer than oxide solid-state lithium electrolytes such as  $\text{Li-La}_3\text{Zr}_2\text{O}_{12}$  ( $B_{\text{DFT}} = 117$  GPa,

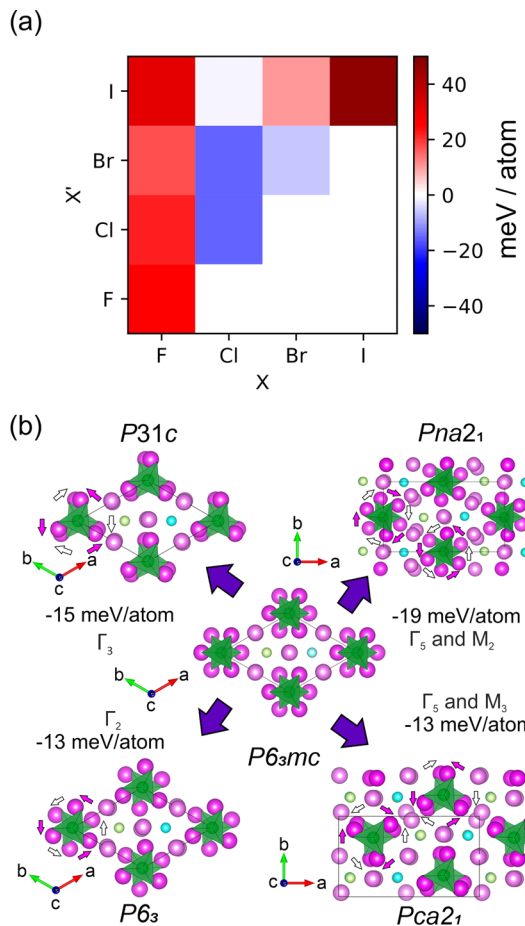


**Figure 3.** (a) Stabilities of the compounds  $\text{Li}_6\text{SiO}_4\text{XX}'$  ( $\text{X}/\text{X}' = \text{F}^-, \text{Cl}^-, \text{Br}^-, \text{I}^-$ ) against decomposition into  $\text{Li}_4\text{SiO}_4 + \text{LiX} + \text{LiX}'$ , calculated using DFT.  $\text{Li}_6\text{SiO}_4\text{BrCl}$  and  $\text{Li}_6\text{SiO}_4\text{Cl}_2$  are calculated to be the most stable compositions. (b) DFT-optimized structures of  $\text{Li}_6\text{SiO}_4\text{Cl}_2$  (Li: pink,  $\text{SiO}_4$ : green, Cl: light green and blue). In the high-symmetry  $P6_3mc$  structure (center), half of the lithium ions lie on mirror planes (shown in darker pink). Displacement of these lithium ions off the mirror planes leads to a lowering of symmetry and a reduction in the DFT-calculated energy. Triangles of lithium ions are displaced by small rotations about the  $c$  axis. These rotations can be in phase or out of phase, leading to the different low-symmetry structures shown. Rotations of lithium ions in the  $\text{Li}_3\text{SiO}_4$  layers and  $\text{Li}_3\text{Cl}$  layers are shown by pink and white arrows, respectively.

**Table 1. Computed Decomposition Energies of the Compounds  $\text{Li}_6\text{SiO}_4\text{XX}'$  in the Most Stable Symmetry**

composition	energy meV/atom	symmetry
$\text{Li}_6\text{SiO}_4\text{Cl}_2$	-18	$Pna2_1$
$\text{Li}_6\text{SiO}_4\text{ClBr}$	-16	$Pna2_1$
$\text{Li}_6\text{SiO}_4\text{Br}_2$	-6	$Pna2_1$
$\text{Li}_6\text{SiO}_4\text{ClI}$	-2	$P6_3mc$

$G_{\text{DFT}} = 64 \text{ GPa}$ <sup>19</sup> and has mechanical properties closer to that of the lithium antiperovskites (e.g.,  $\text{Li}_3\text{OBr}$ ,  $B_{\text{DFT}} = 50.6 \text{ GPa}$ ,  $G_{\text{DFT}} = 37 \text{ GPa}$ ).  $\text{Li}_6\text{SiO}_4\text{Cl}_2$  is stiffer than related sulfide compounds (e.g.,  $\text{Li}_6\text{PS}_5\text{Br}$ :  $B_{\text{DFT}} = 27 \text{ GPa}$ ,  $G_{\text{DFT}} = 14 \text{ GPa}$ ) and consequently easily meets the Monroe–Newman criterion for the prevention of dendrite growth.<sup>47</sup> Future electrolytes based on these mixed oxide/halide compounds may thus be able to overcome some of the processing challenges and

mechanical stability issues inherent in the use of pure oxide and sulfide ceramics.<sup>48</sup>

### 3.2. Synthesis, Thermal Behavior, and Structure Determination.

Compounds were synthesized as powders with compositions  $\text{Li}_6\text{SiO}_4\text{Cl}_{2-x}\text{Br}_x$  ( $x = 0, 0.5, 1$ ) to explore the computationally predicted targets. Synthesis of powders was attempted at varying reaction temperatures (50 K steps from 723 to 873 K) and reaction times (12, 24, 48 h), and starting materials and resulting powders were handled under an argon atmosphere and annealed in alumina crucibles in evacuated silica ampoules (Section 2.2). Synthesis at 823 K for 48 h yielded phase-pure powders for  $\text{Li}_6\text{SiO}_4\text{Cl}_2$ . This new phase persists in the compositional range  $\text{Li}_6\text{SiO}_4\text{Cl}_{2-x}\text{Br}_x$  ( $0 \geq x \geq 1$ ) and displays increased lattice parameters as a function of bromine content (Figure S1). Despite this clear indication of anion substitution, all compositions with  $x > 0$  contained impurities; only  $\text{Li}_6\text{SiO}_4\text{Cl}_2$  was synthesized as a phase-pure white powder, and as such, all further discussion therefore concerns  $\text{Li}_6\text{SiO}_4\text{Cl}_2$ . Single crystals of  $\text{Li}_6\text{SiO}_4\text{Cl}_2$  were synthesized by annealing at 883 K for 3 h before slow cooling ( $3 \text{ K h}^{-1}$ ) to room temperature. High-resolution synchrotron XRD data (SXRD) were collected on the powder from 298 to 798 K in 25 K steps. At temperatures 473–498 K, convergence of some peaks and disappearance of other small peaks indicate a phase transition to a high-temperature, higher-symmetry phase (denoted HT phase) (Figure 4a,b). This transition is also observed in differential scanning calorimetry (DSC) data measured from  $\text{Li}_6\text{SiO}_4\text{Cl}_2$  powder, which shows endothermic and exothermic events on heating and cooling, respectively, associated with this reversible phase transition (Figure 4c). The exact transition temperature determined from DSC data is  $469.3(1)$  K, consistent with the observations from SXRD, NMR, and AC impedance measurements (see below). Similarly to the RT phase, the experimental SXRD pattern of the HT phase could not be indexed to any known compounds in the Li–Si–O–Cl phase field. The structure of the RT phase was solved by single-crystal (SC) X-ray diffraction and the HT phase by the Rietveld refinement of a computed starting model against high-resolution SXRD data.

**3.2.1. Room-Temperature Phase: Structure Determination.** The crystal structure was solved in the space group  $Pna2_1$  from a nonmerohedrally twinned crystal with lattice parameters:  $a = 10.5204(8) \text{ \AA}$ ,  $b = 6.0756(4) \text{ \AA}$ , and  $c = 9.9530(7) \text{ \AA}$ . The assignments of Li, Si, O, and Cl were determined based on interatomic distances and relative displacement parameters. All atomic positions were refined with fixed fully occupied sites. Lithium atoms exhibited nonpositive definite anisotropic mean square displacements, so ISOR restraints were applied to atoms Li1–6 during the final refinement and also to atoms O2–4 as a result of distorted thermal ellipsoids. The final anisotropic atomic refinement converged to  $R_1 = 0.0530$ ,  $wR_2 = 0.1189$  for reflections with  $I \geq 2\sigma(I)$  and  $R_1 = 0.0750$ ,  $wR_2 = 0.1279$  for all reflections. Crystallographic data and structural refinements for  $\text{Li}_6\text{SiO}_4\text{Cl}_2$  are summarized in Table S2. The asymmetric unit contains two distinct crystallographic Cl positions, four distinct O positions, one Si position (further confirmed by  $^{29}\text{Si}$  solid-state NMR, which displays a main signal at  $-67 \text{ ppm}$ , Figure S2, corresponding to a  $\text{SiO}_4^{4-}$  unit), and six Li positions. The final refined atomic positions, and isotropic and anisotropic displacement parameters of each atom are given in Tables S3 and S4, and the selected bond lengths and angles are given in Tables S5 and S6. Orthorhombic superlattice reflections characteristic of the

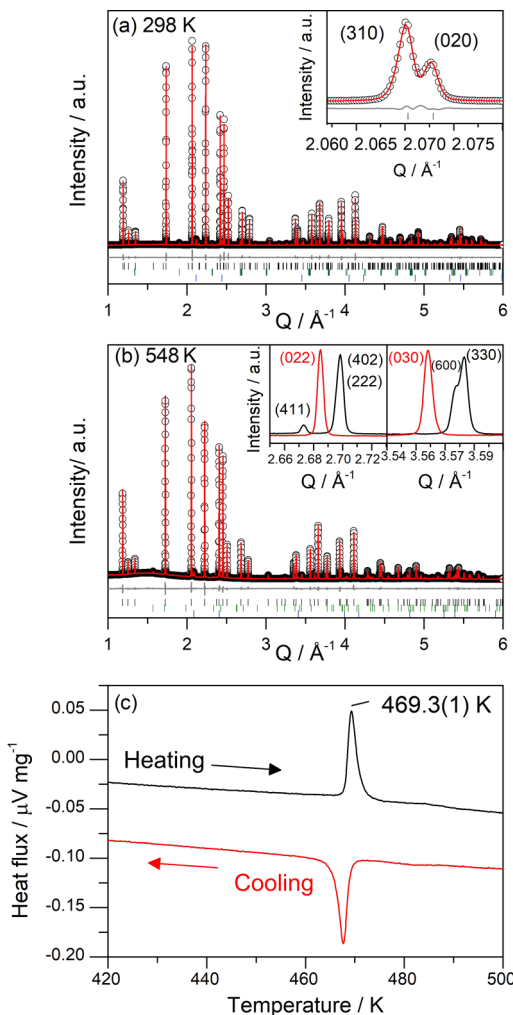


**Figure 4.** (a) RT- $\text{Li}_6\text{SiO}_4\text{Cl}_2$ : Rietveld refinement against SXRD of RT- $\text{Li}_6\text{SiO}_4\text{Cl}_2$  (Diamond Light Source I11 beamline) with  $I_{\text{obs}}$  (black circles),  $I_{\text{calc}}$  (red line),  $I_{\text{obs}} - I_{\text{calc}}$  (gray line), and Bragg reflections (black tick marks for  $\text{Li}_6\text{SiO}_4\text{Cl}_2$ , green tick marks for  $\text{Li}_2\text{SiO}_3$ , blue tick marks for  $\text{LiCl}$ ); the inset highlights reflections consistent with the orthorhombic  $Pna2_1$  symmetry. (b) HT- $\text{Li}_6\text{SiO}_4\text{Cl}_2$ : Rietveld refinement against SXRD data of  $\text{Li}_6\text{SiO}_4\text{Cl}_2$  (black tick marks for  $\text{Li}_6\text{SiO}_4\text{Cl}_2$ , green tick marks for  $\text{LiAlO}_2$ , and blue tick marks for  $\text{LiCl}$ ); the inset compares reflections from the RT-orthorhombic phase at 298 K (black line) with the HT-hexagonal phase at 548 K (red line). (c) Differential scanning calorimetry (DSC) data showing a reversible thermal event associated with phase transition between  $Pna2_1$  and  $P6_3mc$  symmetries in  $\text{Li}_6\text{SiO}_4\text{Cl}_2$ .

$Pna2_1$  (e.g., (411)) symmetry are clearly visible in the diffraction image, ruling out possible C-centered orthorhombic or hexagonal (as  $a \approx \sqrt{3}b$ ) supergroups.

The high-resolution room-temperature SXRD data further confirms this model showing subtle peak splitting consistent with the  $Pna2_1$  symmetry (Figure 4a, inset) evident due to higher  $Q$  resolution in the synchrotron data.

The observed systematic absences in the SXRD data were consistent with the  $Pna2_1$  space group and the lattice parameters refined to  $a = 10.543155(5)$  Å,  $b = 6.07657(3)$  Å, and  $c = 9.960255(5)$  Å from a Pawley fit. The model obtained from SC diffraction proved to be a good starting point for the Rietveld refinement with values of  $R_{\text{wp}} = 4.61$  and  $\chi^2 = 2.81$  after the initial refinement of site occupancies and displacement parameters. Cl and O site occupancies were

refined, and Li site occupancies were fixed to achieve charge neutrality. Refinement of atomic positions improved  $R_{\text{wp}}$  from 4.61 to 4.27 and  $\chi^2$  from 2.81 to 2.61 (Figure S3). Small impurity phases of  $\text{LiCl}$  (1.95%) and  $\text{Li}_2\text{SiO}_3$  (2.35%) were observed (Figure S4a). The maximum entropy method (MEM) analysis did not show any additional electron density, indicating that all lithium sites are accounted for in the structural model described above (Figure S6). The final Rietveld fit is shown in Figure 4a, and refined structural parameters are presented in Tables S7 and S8. The refined composition is  $\text{Li}_{5.957(2)}\text{Si}_{1.00}\text{O}_{3.986(2)}\text{Cl}_{1.985(1)}$ , and the RT phase will therefore be denoted RT- $\text{Li}_6\text{SiO}_4\text{Cl}_2$  hereafter for simplicity.

**3.2.2. Room-Temperature Phase: Structure Description.** As described in Section 3.1, the orthorhombic structure arises from the rotation of lithium atoms off the mirror plane in  $P6_3mc$  through activation of  $\Gamma_5$  and  $M_2$  modes, stabilizing the  $Pna2_1$  symmetry. This leads to a change in anionic and cationic coordination environments compared to the hexagonal defect antiperovskite parent.

The experimentally determined RT structure is shown in Figure 5a, highlighting the atomic packing within the structure defined by alternating  $\text{Li}_6\text{SiO}_4$  and  $\text{Li}_3\text{Cl}$  layers. Comparison of the experimentally determined  $Pna2_1$  structure to the computed structure shows almost identical atomic positions (Figure S7a). The chloride ions that occupy 50% of the antiperovskite B-site positions (Cl1) are found in an octahedral environment with bond lengths ranging from 2.415(3) to 2.621(3) Å to neighboring Li. Compared to the idealized octahedral environment expected for B-site anions in antiperovskites, the octahedra are distorted slightly as a result of the nonrigid rotation of Li ions and the displacement of chlorine toward neighboring vacant B-sites. The chloride ions that occupy 50% of the A-site (Cl2), typically forming cuboctahedral (12-fold) coordination environments in hexagonal perovskites such as 4H-BaMnO<sub>3</sub>, occupy a distorted octahedral environment in the orthorhombic polymorph with bond lengths from 2.446(3) to 2.798(7) Å (Figure S8). All lithium atoms are found in tetrahedral  $\text{LiCl}_2\text{O}_2$  coordination environments. Due to the difference in ionic radii ( $r_{\text{Cl}} = 1.81$  Å,  $r_{\text{O}} = 1.40$  Å),<sup>45</sup> lithium atoms are displaced toward the oxygen atoms (Figure 5c). Li–O bond lengths vary from 1.829(3) to 1.931(3) Å, comparable to distances reported for the cubic argyrodite  $\text{Li}_6\text{PO}_5\text{Cl}$  (1.93 Å)<sup>9</sup> and shorter than Li–O bonds in  $\text{Li}_4\text{SiO}_4$  (1.84–2.51 Å).<sup>49</sup> Li–Cl bond lengths range from 2.415(3) to 2.798(3) Å. These values are larger than expected for typical  $\text{LiCl}_4$  bond lengths, e.g., 2.38 Å in  $\text{Li}_2\text{MgCl}_4$ .<sup>50</sup> The difference in bond lengths compared to homoleptic  $\text{LiCl}_4$  and  $\text{LiO}_4$  tetrahedral environments is expected in heteroleptic  $\text{LiCl}_2\text{O}_2$  and optimizes the bond valence sum for  $\text{Li}^+$  (BVS: 0.939(8)–1.12(1)). The Li–Cl distances in  $\text{Li}_6\text{SiO}_4\text{Cl}_2$  are shorter than in the cubic oxide argyrodite  $\text{Li}_6\text{PO}_5\text{Cl}$  (2.910(4) Å), in which Li atoms have a trigonal bipyramidal coordination ( $\text{LiO}_3\text{Cl}_2$ ) with Cl occupying the axial positions.<sup>9</sup>

In the RT structure,  $\text{LiCl}_2\text{O}_2$  tetrahedra are connected through the corner-sharing of Cl and O vertices and the sharing of Cl–Cl edges; they are referred to using the central lithium atom, i.e.,  $\text{Li}(1)\text{O}_2\text{Cl}_2$  as a Li1 tetrahedron. Edge-sharing between Li1–Li3 and Li4–Li6 tetrahedra is facilitated by the lithium-ion displacements away from the shared Cl–Cl edges (Figure 6a,c), minimizing electrostatic repulsions.

The  $\text{Li}_6\text{SiO}_4$  layer can be described (Figure 6a) as alternating corner-sharing Li2–Li3 and Li1–SiO<sub>4</sub> chains

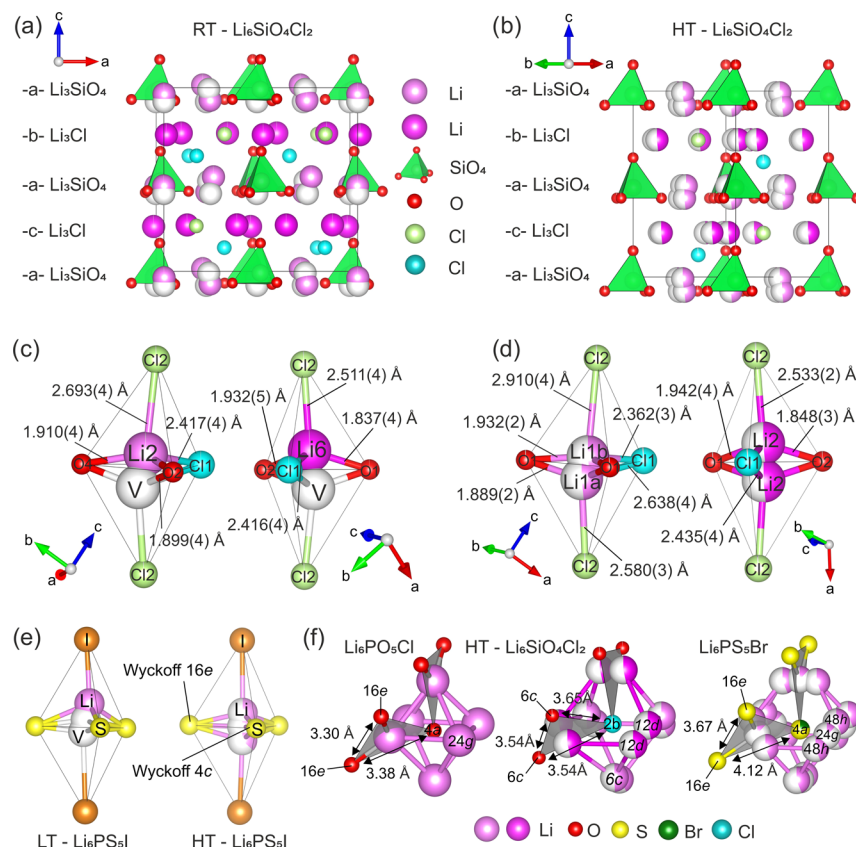


**Figure 5.** (a) RT- $\text{Li}_6\text{SiO}_4\text{Cl}_2$  unit cell showing alternating  $\text{Li}_3\text{Cl}$  and  $\text{Li}_3\text{SiO}_4$  layers. Comparing with the  $\text{ABX}_3$  perovskite,  $\text{SiO}_4$  (green tetrahedra) and  $\text{Cl}_2$  (light green) occupy the A-sites,  $\text{Cl}1$  (blue) ions fill 50% of the B-sites with the remaining 50% vacant, and lithium atoms occupy the X-sites ( $\text{Li}1$ ,  $\text{Li}2$ ,  $\text{Li}3$  atoms in light pink,  $\text{Li}4$ ,  $\text{Li}5$ ,  $\text{Li}6$  atoms in dark pink). Vacant tetrahedral lithium sites in the  $\text{Li}_3\text{SiO}_4$  layer are shown in white to facilitate comparison with the HT structure. (b) HT- $\text{Li}_6\text{SiO}_4\text{Cl}_2$  unit cell showing the same alternating  $\text{Li}_3\text{Cl}$  and  $\text{Li}_3\text{SiO}_4$  layers. Lithium atoms are disordered over partially occupied sites with respect to the RT structure ( $\text{Li}1\text{a}$  and  $\text{Li}1\text{b}$  atoms in light pink,  $\text{Li}2$  atoms in dark pink). (c) RT- $\text{Li}_6\text{SiO}_4\text{Cl}_2$  lithium tetrahedra showing displacement of lithium (4a Wyckoff site) toward coordinating oxygen. The vacant tetrahedral sites (V), drawn in white, are generated by activation of occupational modes when lowering the symmetry of HT- $\text{Li}_6\text{SiO}_4\text{Cl}_2$  to  $Pna_2_1$  through ISODISTORT (Figure S10). (d) HT- $\text{Li}_6\text{SiO}_4\text{Cl}_2$   $\text{Li}1\text{a}$ ,  $\text{Li}1\text{b}$  (6c Wyckoff site), and  $\text{Li}2$  (12d Wyckoff site) coordination environment, showing partial occupancy of tetrahedral sites that are both fully occupied and vacant at RT. (e) This order-disorder behavior of lithium sites is analogous to the lithium distribution in  $\text{Li}_6\text{PS}_5\text{I}$  argyrodite;<sup>21</sup> at low temperatures (LTs), lithium atoms are ordered occupying one of the tetrahedral positions, whereas at high-temperature (HT), lithium ions are disordered with partial occupancy of tetrahedral and trigonal positions. Distinct sulfide anion positions are labeled in the HT structure. (f) Octahedral Li-ion cages surrounding B-site anions in  $\text{Li}_6\text{PO}_5\text{Cl}$  (cubic), HT- $\text{Li}_6\text{SiO}_4\text{Cl}_2$  (hexagonal), and  $\text{Li}_6\text{PS}_5\text{Br}$  (cubic). Trigonal anion windows (consisting of three oxide anions in  $\text{Li}_6\text{PO}_5\text{Cl}$ , two oxide anions and one chloride anion in  $\text{Li}_6\text{SiO}_4\text{Cl}_2$ , and two sulfide and one mixed sulfide/bromide site in  $\text{Li}_6\text{PS}_5\text{Br}$ ) are shown, highlighting their anion-anion distances that determine the window area. Two distinct trigonal windows are present in HT- $\text{Li}_6\text{SiO}_4\text{Cl}_2$ , with oxide ions both either occupying Wyckoff position 6c (edge length: 3.54 Å) or occupying Wyckoff positions 2a and 6c (edge length: 3.23 Å). Lithium ions move through these windows in argyrodite solid electrolytes.

running along  $b$ , connected in the  $a$ -direction by  $\text{Li}1-\text{Li}2$ ,  $\text{SiO}_4-\text{Li}2$ ,  $\text{SiO}_4-\text{Li}3$  corner-sharing, and  $\text{Li}1-\text{Li}3$  edge-sharing (Figure 6b,c).  $\text{Cl}2$  atoms located in the  $\text{Li}_3\text{Cl}$  layers connect  $\text{Li}_3\text{SiO}_4$  layers along the stacking  $c$ -direction (Figure 6b). The  $\text{Li}_3\text{Cl}$  layer is made up of  $\text{Li}4$ ,  $\text{Li}5$ , and  $\text{Li}6$  tetrahedra connected through  $\text{Li}4-\text{Li}5$ ,  $\text{Li}4-\text{Li}6$ ,  $\text{Li}5-\text{Li}6$  corner-sharing, and  $\text{Li}4-\text{Li}6$  edge-sharing (Figure 6c,d). The  $\text{Li}_3\text{Cl}$  layer is connected to the  $\text{Li}_3\text{SiO}_4$  layer through corner-sharing with  $\text{Li}1$ ,  $\text{Li}2$ ,  $\text{Li}3$ , and  $\text{SiO}_4$  tetrahedra, forming the three-dimensional (3D)-network of corner- and edge-shared tetrahedra.

**3.2.3. High-Temperature Phase: Structure Determination.** Indexing of the HT phase (above 523 K) with TOPAS resulted in a hexagonal unit cell with lattice parameters  $a = 6.11 \text{ \AA}$  and  $c = 10.02 \text{ \AA}$ . Systematic absences in the powder pattern were consistent with the  $P31c$  and  $P6_3mc$  space groups, agreeing with the computationally stable hexagonal structures (Section

3.1 and Figure 3c). Very similar Pawley fits were obtained using these symmetries, and lattice parameters were refined to  $a = 6.110805(12) \text{ \AA}$  and  $c = 10.02068(3) \text{ \AA}$  for  $P6_3mc$  (Figure S4b). The higher-symmetry computed  $P6_3mc$  structure gave a reasonable starting point for the Rietveld refinement. The unit cell contains two distinct crystallographic  $\text{Cl}$  positions (Wyckoff position 2b), two O positions (Wyckoff positions 6c and 2a), one Si position (Wyckoff position 2a), and three Li positions (Wyckoff positions 6c and 12d). Occupancies of Cl and O sites were refined, and the occupancies of Li sites were fixed to ensure charge neutrality. In the computational model,  $\text{Li}2$  is located on the mirror plane in special position 6c (Figure S7b). Inspection of the Fourier density map (FDM) reveals extra electron density around this position and indicates displacement of  $\text{Li}2$  away from the mirror plane onto the general position 12d (Figure S9a). Replacing the 6c site with the 12d position improved  $R_{wp}$  from 3.61 to 2.98%. The FDM

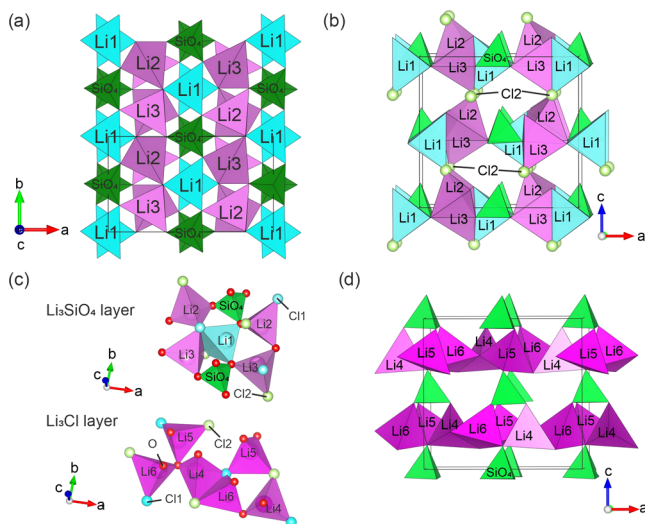


**Figure 6.** (a) Li<sub>3</sub>SiO<sub>4</sub> intralayer environments and Li<sub>2</sub>–Li<sub>3</sub> (pink) and Li<sub>1</sub>–SiO<sub>4</sub> (blue and green, respectively) chains of corner- and edge-sharing tetrahedra. (b) Connection of Li<sub>3</sub>SiO<sub>4</sub> layers along the stacking axis (c) through corner-sharing of Cl<sub>2</sub> atoms (light green). (c) Li<sub>3</sub>SiO<sub>4</sub> (top) and Li<sub>3</sub>Cl (bottom) layers consisting of corner- and edge-sharing tetrahedra (Li<sub>1</sub>: light blue, Li<sub>2</sub>, Li<sub>3</sub>: light pink, Li<sub>4</sub>–Li<sub>6</sub>: dark pink, Si: green, Cl<sub>1</sub> (B-sites): blue, Cl<sub>2</sub> (A-sites): light green, O: red), all shared edges are Cl–Cl. (d) Li<sub>3</sub>Cl layers connected via SiO<sub>4</sub> units viewed along the b-direction showing stacking along c; SiO<sub>4</sub> tetrahedra are shown to guide the eye.

also revealed electron density around the Li<sub>1</sub> position along the c-direction (Figure S9b). Splitting the Li<sub>1</sub> site into two distinct Li<sub>1a</sub> and Li<sub>1b</sub> sites along c further improved  $R_{wp}$  to 2.75%. The computed P31c model (Figure 3c) is similar, only allowing two distinct 6c crystallographic sites for Li<sub>2</sub> instead of one 12d site. A fit of the diffraction data to this model, with independent refinement of both Li<sub>2a</sub> and Li<sub>2b</sub> 6c occupancies, did not result in an improved fit. The P6<sub>3</sub>mc model was therefore used for final refinement. MEM analysis also supports the displacement of Li<sub>1</sub> and Li<sub>2</sub> positions (Figure S6). The final refinement is shown in Figure 4b, and the refined structural parameters are provided in Table S7. The refined composition is Li<sub>5.82(4)</sub>Si<sub>1.00</sub>O<sub>3.934(6)</sub>Cl<sub>1.956(4)</sub>, and the HT phase will therefore be denoted HT-Li<sub>6</sub>SiO<sub>4</sub>Cl<sub>2</sub> hereafter for simplicity.

**3.2.4. High-Temperature Phase: Structure Description.** The HT P6<sub>3</sub>mc structure can be described as a 4H-hexagonal antiperovskite of general formula ABX<sub>3</sub>, with structural similarities to 4H-BaMnO<sub>3</sub> (Figure 2b) in which half of the B-sites are vacant. This is consistent with cation-deficient hexagonal perovskites with the formula A<sub>2</sub>BX<sub>6</sub>, such as Rb<sub>2</sub>MnF<sub>6</sub> with the P6<sub>3</sub>mc symmetry.<sup>51</sup> The HT structure of Li<sub>6</sub>SiO<sub>4</sub>Cl<sub>2</sub>, consisting of alternating hexagonally stacked Li<sub>3</sub>Cl and Li<sub>3</sub>SiO<sub>4</sub> layers, is shown in Figure 5b. The (poly)anion network in the HT structure remains unchanged through the phase transition from the RT structure, with the observed symmetry change originating from displacements in Li positions. The lithium environments remain tetrahedral (LiO<sub>2</sub>Cl<sub>2</sub>) with lithium atoms displaced toward the oxygens due to its smaller ionic radius compared to chlorine. Li–Cl bond lengths vary from 2.366(3) to 2.908(8) Å, and Li–O bond lengths range from 1.847(4) to 1.942(4) Å (Figure 5d).

As shown in Figure 5c,d, the ordered lithium atoms of RT-Li<sub>6</sub>SiO<sub>4</sub>Cl<sub>2</sub> are disordered in the higher-symmetry HT

structure. Similar to the results from normal mode calculations described in Section 3.1, this order–disorder transition occurs via activation of occupational M<sub>2</sub> and Γ<sub>5</sub> modes, with a small contribution from displacive Γ<sub>5</sub> modes that predominantly involve displacement of the Li<sub>1</sub> atoms within the close-packed Li<sub>3</sub>SiO<sub>4</sub> layer (Figure S10). This disorder of the A cation positions is well known in  $A_{(12-n^*-y)/m}^{n^+}L_6^{n^+}X_{6-y}^{2-}Y_y^-$  argyrodites<sup>52,53</sup> and provides a direct comparison of Li disorder between oxide and sulfide argyrodite materials. The delocalization of Li positions in HT-Li<sub>6</sub>SiO<sub>4</sub>Cl<sub>2</sub> resembles that observed in high-temperature F43m cubic argyrodites Li<sub>6</sub>PS<sub>5</sub>X (X = Cl, Br, I), in which Li partially occupies both tetrahedral and trigonal planar coordination environments (48h and 24g Wyckoff sites, respectively; Figure S9c) and is one of the reasons for reduced energy barriers for bulk Li-ion transport in these materials.<sup>8</sup>

The order–disorder transition of Li<sub>6</sub>SiO<sub>4</sub>Cl<sub>2</sub> (Figure 5c,d) is similar to the behavior of many argyrodites; Cu<sub>8</sub>GeSe<sub>6</sub> displays an order–disorder transition between P6<sub>3</sub>cm and P6<sub>3</sub>mc structures, where Cu ions are disordered in the latter similarly to Li on the 6c and 12d Wyckoff positions in Li<sub>6</sub>SiO<sub>4</sub>Cl<sub>2</sub>,<sup>39,54</sup> and analogous behavior is observed in silver-containing argyrodites.<sup>1</sup> Specifically, cubic Li<sub>6</sub>PS<sub>5</sub>I has ordered lithium positions at low temperature (<180 K) and a disordered structure at 298 K in which lithium is delocalized across the 24g and 48h positions (Figure 5e),<sup>21</sup> resulting in comparable local lithium coordination environments with Li<sub>6</sub>SiO<sub>4</sub>Cl<sub>2</sub> (Figure 5c,d) that are consistent with dynamical disorder. This is distinct from the cubic oxide argyrodite, Li<sub>6</sub>PO<sub>5</sub>Br, in which lithium remains localized on the trigonal planar 24g Wyckoff position in the F43m structure over a wide (173–873 K) temperature range (Figure 1e).<sup>48</sup> Stabilization of this lithium disorder, which enables access to higher-energy sites in Li<sub>6</sub>SiO<sub>4</sub>Cl<sub>2</sub>, would increase lithium-ion migration compared against the room-temperature structure.

**3.3. Transport Properties.** The ionic conductivity of Li<sub>6</sub>SiO<sub>4</sub>Cl<sub>2</sub> was investigated through AC impedance spectroscopy on a sintered white pellet of ~84% theoretical density (pellet cold-pressed under 125 MPa and sintered in an evacuated silica ampoule for 12 h at 848 K). A typical set of data measured at 533 K in an inert atmosphere are shown in Figure 7a. The impedance complex plane plots, Z\*, consist of a high-frequency arc with the presence of a small low-frequency inclined spike. The large single arc is attributed to the sample bulk, as shown by overlapping peaks in the combined Z'/M'' spectra (Figure S12a). The associated capacitance of the high-frequency arc, 0.6 pF cm<sup>-1</sup>, corresponding to a permittivity of ~6.8, is also consistent with the grain response (Figure S12b). The low-frequency spike is attributed to the double-layer capacitance at the blocking sample–electrode interface, where Li ions cannot pass. To a first approximation, the high-frequency arc could be modeled with an equivalent circuit consisting of a resistor in parallel with a constant phase element (CPE). Impedance data were fitted to the equivalent circuit using ZView software (Figure 7a). In general, the material is homogeneous and shows a total conductivity of 6.2 × 10<sup>-6</sup> S cm<sup>-1</sup> at 575 K and ~10<sup>-10</sup> S cm<sup>-1</sup> at room temperature. DC polarization measurements show a low electronic contribution of >0.5% at 300 °C to the overall conductivity (eq 1 and Figure S13). From the low-frequency intercept of the impedance arc on the Z' axis, the values of the total resistance were obtained and are shown in an Arrhenius format in Figure 7b. A change in slope can be observed above

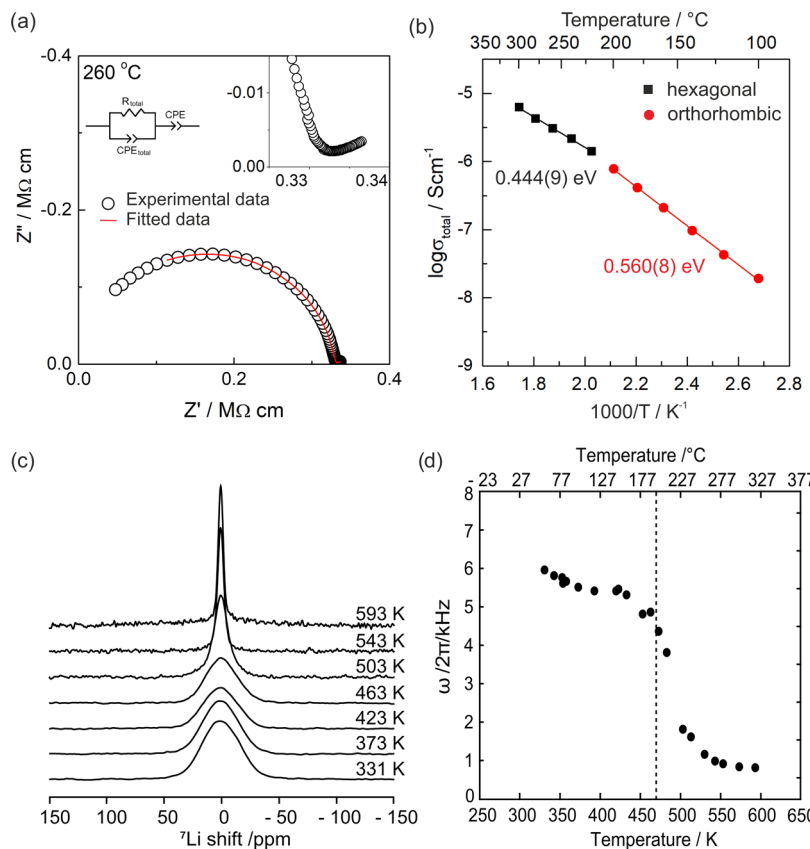


**Figure 7.** (a) Impedance complex plane plots  $Z^*$  of  $\text{Li}_6\text{SiO}_4\text{Cl}_2$  at 533 K; the inset shows equivalent circuit used to model the data. The inset shows the low-frequency inclined spike attributed to the capacitance of the blocking electrode. (b) Arrhenius plots of the total conductivity; activation energies derived from the data are shown. A change in Arrhenius behavior and activation energy can be seen at  $\sim 470$  K corresponding to the phase change observed in VT-XRD and DSC measurements. (c)  ${}^7\text{Li}$  NMR spectra under static conditions as a function of temperature. (d) Motional narrowing of the line width (full width at half-maximum) of the central  ${}^7\text{Li}$  NMR transition. The temperature at which the phase change is detected via DSC measurements is also noted (dashed line).

$\sim 498$  K, agreeing with the phase transition observed via VT-XRD and DSC experiments. The orthorhombic phase (red circles) and the hexagonal phase (black squares) have activation energies of 0.560(8) and 0.444(9) eV, respectively.

The local ionic mobility of lithium was investigated through  ${}^7\text{Li}$  solid-state NMR. The temperature dependence of the static  ${}^7\text{Li}$  NMR spectra of  $\text{Li}_6\text{SiO}_4\text{Cl}_2$  over the temperature range of 331–593 K is shown in Figure 7c. At temperatures where ion mobility is minimal, i.e., the rigid lattice regime, the  $1/2 \leftrightarrow -1/2$  central transition is broadened by the  ${}^7\text{Li}-{}^7\text{Li}$  homonuclear dipolar coupling. For  $\text{Li}_6\text{SiO}_4\text{Cl}_2$ , this region is between 350 and 450 K, where the line width of the central transition is  $\sim 5.5$  kHz. As the temperature is increased above 450 K, the line width decreases drastically over a small temperature range (Figure 7d) due to the increasing motion of the Li spins continuously averaging the dipolar interactions and clearly evidences an increase in ionic mobility facilitated by the phase transition from the ordered RT-orthorhombic to the higher-symmetry HT-hexagonal phase.

Through calculation of the strength of  ${}^7\text{Li}-{}^7\text{Li}$  homonuclear dipolar coupling of both the room-temperature and high-temperature phases of  $\text{Li}_6\text{SiO}_4\text{Cl}_2$ , further insight into the local ion dynamics of the two phases can be determined. By extracting the shortest Li–Li distance from the SXRD data (Li1–Li5, 2.697(6) Å), the absolute value of the dipolar coupling constant can be calculated (eq 2) as  $\sim 5.8$  kHz in RT- $\text{Li}_6\text{SiO}_4\text{Cl}_2$  in full agreement with the experimental line width

observed, while  $\sim 8.2$  kHz is obtained from Li1a and Li2 (2.410(5) Å) for HT- $\text{Li}_6\text{SiO}_4\text{Cl}_2$ . Due to the increase in dipolar coupling after the phase transition, it would be expected that  ${}^7\text{Li}$  spectra demonstrate increased line widths at higher T in the absence of an increase in Li-ion mobility. However, the line narrowing observed (Figure 7d) is a clear indication that the phase transition from the RT-orthorhombic phase to the higher-symmetry HT-hexagonal phase facilitates an increase in Li-ion mobility, as also observed in AC impedance measurements (Figure 7b). The delocalization of lithium in HT- $\text{Li}_6\text{SiO}_4\text{Cl}_2$  across the 6c and 12d sites (Figure 5c,d) results in a lowering of the activation energy from RT- $\text{Li}_6\text{SiO}_4\text{Cl}_2$  where the lithium positions are fully ordered. The activation energies obtained from  $\text{Li}_6\text{SiO}_4\text{Cl}_2$  are lower than those extracted from  $\text{Li}_6\text{PO}_5\text{Cl}$  across the measured temperature range, despite the latter adopting the higher-symmetry cubic  $F\bar{4}3m$  structure.<sup>9</sup>

The distinction between the oxide materials  $\text{Li}_6\text{SiO}_4\text{Cl}_2$  and  $\text{Li}_6\text{PO}_5\text{Cl}$  is likely the increased size of the trigonal anion window (Figure 5f) and the associated dynamical Li disorder (absent in cubic  $\text{Li}_6\text{PO}_5\text{Cl}$ , where Li is localized on the 24g position) in hexagonal  $\text{Li}_6\text{SiO}_4\text{Cl}_2$  (partial occupancy of 6c and 12d positions by Li), leading to lower activation energies for ion mobility. Local jumps of  $\text{Li}^+$  between these tetrahedral sites separated by the trigonal anion windows are the most favorable for ionic diffusion in argyrodites.<sup>8</sup> Occupational disorder via chalcogenide–halide mixing on the anion position that forms

part of the trigonal window that mobile cations traverse (Figure 5f) is an important route to enhancing Li-ion mobility.<sup>12,54</sup> Unlike  $\text{Li}_6\text{PO}_5\text{Cl}$ , where this window is formed from three oxide anions, the  $\text{LiCl}_2\text{O}_2$  environments of  $\text{Li}_6\text{SiO}_4\text{Cl}_2$  yield a window described by one chloride and two oxide anions. The larger Cl ( $r_{\text{Cl}} = 1.81 \text{ \AA}$ ,  $r_{\text{O}} = 1.40 \text{ \AA}$ )<sup>45</sup> increases the size of this window, further lowering the activation energy of ion transport compared to  $\text{Li}_6\text{PO}_5\text{Cl}$ .

## 4. CONCLUSIONS

The connection between argyrodite and antiperovskite structures is established, thus identifying close-packed layers that can be assembled through the diversity of combined hexagonal and cubic stacking operations known to give the perovskite material family its breadth of scientific and technological importance. We exemplify these mixed stackings in the hexagonal argyrodite material family through the prediction and then isolation of the nontoxic and earth-abundant  $\text{Li}_6\text{SiO}_4\text{Cl}_2$ . Here, the resulting layer stacking gives access to a disordered Li distribution, which is observed in fast lithium-ion conductors, a distribution not accessible to its nearest known cubic compositional counterpart,  $\text{Li}_6\text{PO}_5\text{Cl}$ . Exploration of the many accessible mixed layer sequences and associated site and chemical orderings afforded within this family opens new routes to the tuning and creation of ion transport pathways through variation of both composition and structure, as well as broader functional outcomes based on the importance of the cubic argyrodite materials.

## ■ ASSOCIATED CONTENT

### SI Supporting Information

The Supporting Information is available free of charge at <https://pubs.acs.org/doi/10.1021/acs.chemmater.1c00157>.

Computed decomposition energies of the compounds  $\text{Li}_6\text{SiO}_4\text{XX}'$  (X = F, Cl, Br, I) for different space groups, PXRD patterns for  $\text{Li}_6\text{SiO}_4\text{Cl}_{2-x}\text{Br}_x$ , Pawley fits (RT and HT phases), comparison of Rietveld refinement before and after refinement of atomic positions as well as with and without Li atoms (RT phase), MEM analysis (RT and HT phases), comparison of computed and experimental structures (RT and HT phases), Fourier difference map (HT phase), structural information of  $\text{Li}_6\text{SiO}_4\text{Cl}_2$  determined by single-crystal diffraction and powder diffraction refinement (refinement details, atomic positions, bond distances, and angles),  $^{29}\text{Si}$  NMR spectrum and impedance results are available ([PDF](#))

Crystal structure of SC- $\text{Li}_6\text{SiO}_4\text{Cl}_2$  is deposited with ICSD 2032155 ([CIF](#))

Crystallographic data (RT- $\text{Li}_6\text{SiO}_4\text{Cl}_2$ -powder-responses) ([CIF](#))

Crystallographic data (HT- $\text{Li}_6\text{SiO}_4\text{Cl}_2$ ) ([CIF](#))

## ■ AUTHOR INFORMATION

### Corresponding Author

Matthew J. Rosseinsky – Department of Chemistry, University of Liverpool, L69 7ZD Liverpool, U.K.; [orcid.org/0000-0002-1910-2483](#); Email: [m.j.rosseinsky@liverpool.ac.uk](mailto:m.j.rosseinsky@liverpool.ac.uk)

## Authors

Alexandra Morscher – Department of Chemistry, University of Liverpool, L69 7ZD Liverpool, U.K.

Matthew S. Dyer – Department of Chemistry, University of Liverpool, L69 7ZD Liverpool, U.K.

Benjamin B. Duff – Department of Chemistry and Stephenson Institute for Renewable Energy, University of Liverpool, L69 7ZD Liverpool, U.K.; [orcid.org/0000-0002-7398-5002](#)

Guopeng Han – Department of Chemistry, University of Liverpool, L69 7ZD Liverpool, U.K.

Jacinthe Gamon – Department of Chemistry, University of Liverpool, L69 7ZD Liverpool, U.K.

Luke M. Daniels – Department of Chemistry, University of Liverpool, L69 7ZD Liverpool, U.K.; [orcid.org/0000-0002-7077-6125](#)

Yun Dang – Department of Chemistry, University of Liverpool, L69 7ZD Liverpool, U.K.; [orcid.org/0000-0002-0140-0140](#)

T. Wesley Surta – Department of Chemistry, University of Liverpool, L69 7ZD Liverpool, U.K.; [orcid.org/0000-0002-2882-6483](#)

Craig M. Robertson – Department of Chemistry, University of Liverpool, L69 7ZD Liverpool, U.K.

Frédéric Blanc – Department of Chemistry and Stephenson Institute for Renewable Energy, University of Liverpool, L69 7ZD Liverpool, U.K.; [orcid.org/0000-0001-9171-1454](#)

John B. Claridge – Department of Chemistry, University of Liverpool, L69 7ZD Liverpool, U.K.

Complete contact information is available at:  
<https://pubs.acs.org/10.1021/acs.chemmater.1c00157>

## Notes

The authors declare no competing financial interest.

## ■ ACKNOWLEDGMENTS

We are grateful to the support of the Faraday Institution project “SOLBAT—The Solid-State (Li or Na) Metal-Anode Battery” [grant number FIRG007] for funding Y.D., the studentship of A.M., and partial studentship support of B.B.D., who is also supported by the University of Liverpool. This work used the Cirrus U.K. National Tier-2 HPC Service at EPCC (<http://www.cirrus.ac.uk>) funded by the University of Edinburgh and EPSRC (EP/P020267/1), along with the University of Liverpool HPC cluster, Barkla. We thank EPSRC for funding G.H. and J.G. under EP/N004884 and for funding T.W.S. under EP/R011753/1. M.J.R. thanks the Royal Society for a Research Professor position. This work was carried out with the support of Diamond Light Source, instrument I11 (proposal CY23666).

## ■ REFERENCES

- (1) Kuhs, W.; Nitsche, R.; Scheunemann, K. The argyrodites—A new family of tetrahedrally close-packed structures. *Mater. Res. Bull.* **1979**, *14*, 241–248.
- (2) Wada, H. Crystal structures and silver ionic conductivities of the new compounds  $\text{Ag}_x\text{NbS}_6$ ,  $\text{Ag}_7\text{TaSe}_6$  and  $\text{Ag}_{7-\xi}\text{TaSe}_{6-\xi}\text{I}_\xi$  ( $0.1 \leq \xi \leq 0.5$ ). *J. Alloys Compd.* **1992**, *178*, 315–323.
- (3) Li, L.; Liu, Y.; Dai, J.; Hong, A.; Zeng, M.; Yan, Z.; Xu, J.; Zhang, D.; Shan, D.; Liu, S.; Ren, Z.; Liu, J.-M. High thermoelectric performance of superionic argyrodite compound  $\text{Ag}_8\text{SnSe}_6$ . *J. Mater. Chem. C* **2016**, *4*, 5806–5813.
- (4) Gaudin, E.; Boucher, F.; Petricek, V.; Taulelle, F.; Evain, M. Structures and phase transitions of the  $\text{A}_x\text{PSe}_6$  ( $\text{A} = \text{Ag}, \text{Cu}$ )

- argyrodite-type ionic conductors. II.  $\beta$ -and  $\gamma$ -Cu<sub>7</sub>PSe<sub>6</sub>. *Acta Crystallogr. Sect. B: Struct. Sci.* **2000**, *56*, 402–408.
- (5) Evain, M.; Gaudin, E.; Boucher, F.; Petricek, V.; Taulelle, F. Structures and phase transitions of the A<sub>7</sub>PSe<sub>6</sub> (A = Ag, Cu) argyrodite-type ionic conductors. I. Ag<sub>7</sub>PSe<sub>6</sub>. *Acta Crystallogr. Sect. B: Struct. Sci.* **1998**, *54*, 376–383.
- (6) Rao, R. P.; Adams, S. Studies of lithium argyrodite solid electrolytes for all-solid-state batteries. *Phys. Status Solidi A* **2011**, *208*, 1804–1807.
- (7) Deisereth, H. J.; Kong, S. T.; Eckert, H.; Vannahme, J.; Reiner, C.; Zaiß, T.; Schlosser, M. Li<sub>6</sub>PS<sub>5</sub>X: a class of crystalline Li-rich solids with an unusually high Li<sup>+</sup> mobility. *Angew. Chem.* **2008**, *120*, 767–770.
- (8) Deisereth, H. J.; Maier, J.; Weichert, K.; Nickel, V.; Kong, S. T.; Reiner, C. Li<sub>7</sub>PS<sub>6</sub> and Li<sub>6</sub>PS<sub>5</sub>X (X: Cl, Br, I): Possible Three-dimensional Diffusion Pathways for Lithium Ions and Temperature Dependence of the Ionic Conductivity by Impedance Measurements. *Z. Anorg. Allg. Chem.* **2011**, *637*, 1287–1294.
- (9) Kong, S. T.; Deisereth, H. J.; Maier, J.; Nickel, V.; Weichert, K.; Reiner, C. Li<sub>6</sub>PO<sub>5</sub>Br and Li<sub>6</sub>PO<sub>5</sub>Cl: The first Lithium-Oxide-Aryrodites. *Z. Anorg. Allg. Chem.* **2010**, *636*, 1920–1924.
- (10) De Clerk, N. J.; Rosłoni, I.; Wagemaker, M. Diffusion mechanism of Li argyrodite solid electrolytes for Li-ion batteries and prediction of optimized halogen doping: the effect of Li vacancies, halogens, and halogen disorder. *Chem. Mater.* **2016**, *28*, 7955–7963.
- (11) Kraft, M. A.; Culver, S. P.; Calderon, M.; Böcher, F.; Krauskopf, T.; Senyshyn, A.; Dietrich, C.; Zevalkink, A.; Janek, J., Jr; Zeier, W. G. Influence of lattice polarizability on the ionic conductivity in the lithium superionic argyrodites Li<sub>6</sub>PS<sub>5</sub>X (X = Cl, Br, I). *J. Am. Chem. Soc.* **2017**, *139*, 10909–10918.
- (12) Minafra, N.; Culver, S. P.; Krauskopf, T.; Senyshyn, A.; Zeier, W. G. Effect of Si substitution on the structural and transport properties of superionic Li-argyrodites. *J. Mater. Chem. A* **2018**, *6*, 645–651.
- (13) Zhao, Y.; Daemen, L. L. Superionic conductivity in lithium-rich anti-perovskites. *J. Am. Chem. Soc.* **2012**, *134*, 15042–15047.
- (14) Kresse, G.; Furthmüller, J. Efficient iterative schemes for ab initio total-energy calculations using a plane-wave basis set. *Phys. Rev. B* **1996**, *54*, No. 11169.
- (15) Kresse, G.; Joubert, D. From ultrasoft pseudopotentials to the projector augmented-wave method. *Phys. Rev. B* **1999**, *59*, No. 1758.
- (16) Perdew, J. P.; Burke, K.; Ernzerhof, M. Generalized gradient approximation made simple. *Phys. Rev. Lett.* **1996**, *77*, 3865.
- (17) Perdew, J. P.; Ruzsinszky, A.; Csonka, G. I.; Vydrov, O. A.; Scuseria, G. E.; Constantin, L. A.; Zhou, X.; Burke, K. Restoring the density-gradient expansion for exchange in solids and surfaces. *Phys. Rev. Lett.* **2008**, *100*, No. 136406.
- (18) Ong, S. P.; Richards, W. D.; Jain, A.; Hautier, G.; Kocher, M.; Cholia, S.; Gunter, D.; Chevrier, V. L.; Persson, K. A.; Ceder, G. Python Materials Genomics ( pymatgen): A robust, open-source python library for materials analysis. *Comput. Mater. Sci.* **2013**, *68*, 314–319.
- (19) Deng, Z.; Wang, Z.; Chu, I.-H.; Luo, J.; Ong, S. P. Elastic properties of alkali superionic conductor electrolytes from first principles calculations. *J. Electrochem. Soc.* **2016**, *163*, A67.
- (20) Wortmann, R.; Sitta, S.; Sabrowsky, H. Li<sub>7</sub>O<sub>2</sub>Br<sub>3</sub>—Eine weitere Strukturvariante der neuen Alkalimetallchalcogenidhalogenid-Perowskite/Li<sub>7</sub>O<sub>2</sub>Br<sub>3</sub>—A Further Structure Variant of the New Alkali Metal Chalcogenide Halide Perovskites. *Z. Naturforsch. B* **1989**, *44*, 1348–1350.
- (21) Kong, S. T.; Deisereth, H. J.; Reiner, C.; Gün, Ö.; Neumann, E.; Ritter, C.; Zahn, D. Lithium argyrodites with phosphorus and arsenic: order and disorder of lithium atoms, crystal chemistry, and phase transitions. *Chem. - Eur. J.* **2010**, *16*, 2198–2206.
- (22) Tang, T.; Zhang, Z.; Meng, J.-B.; Luo, D.-L. Synthesis and characterization of lithium silicate powders. *Fusion Eng. Des.* **2009**, *84*, 2124–2130.
- (23) Thompson, S.; Parker, J.; Potter, J.; Hill, T.; Birt, A.; Cobb, T.; Yuan, F.; Tang, C. Beamline I11 at Diamond: A new instrument for high resolution powder diffraction. *Rev. Sci. Instrum.* **2009**, *80*, No. 075107.
- (24) Coelho, A. Whole-profile structure solution from powder diffraction data using simulated annealing. *J. Appl. Crystallogr.* **2000**, *33*, 899–908.
- (25) CrysAlisPro Software System. Version 1.171.38.41; Rigaku Oxford Diffraction Ltd.: Yarnton, Oxfordshire, England, 2015.
- (26) Dolomanov, O. V.; Bourhis, L. J.; Gildea, R. J.; Howard, J. A.; Puschmann, H. OLEX2: a complete structure solution, refinement and analysis program. *J. Appl. Crystallogr.* **2009**, *42*, 339–341.
- (27) Sheldrick, G. M. SHELXT—Integrated space-group and crystal-structure determination. *Acta Crystallogr., Sect. A: Found. Adv.* **2015**, *71*, 3–8.
- (28) Sheldrick, G. M. Crystal structure refinement with SHELXL. *Acta Crystallogr., Sect. C: Struct. Chem.* **2015**, *71*, 3–8.
- (29) Johnson, D. ZView: A Software Program for IES Analysis 3.5 d; Scribner Associates Inc., 2007.
- (30) Brendler, E.; Heine, T.; Hill, A. F.; Wagler, J. A pentacoordinate chlorotrimethylsilane derivative: a very polar snapshot of a nucleophilic substitution and its influence on <sup>29</sup>Si solid state NMR properties. *Z. Anorg. Allg. Chem.* **2009**, *635*, 1300–1305.
- (31) Beckmann, P. A.; Dybowski, C. A thermometer for nonspinning solid-state NMR spectroscopy. *J. Magn. Reson.* **2000**, *146*, 379.
- (32) Becker, K. Temperature dependence of NMR chemical shifts in cuprous halides. *J. Chem. Phys.* **1978**, *68*, 3785–3793.
- (33) Wu, J.; Kim, N.; Stebbins, J. F. Temperature calibration for high-temperature MAS NMR to 913 K: <sup>63</sup>Cu MAS NMR of CuBr and CuI, and <sup>23</sup>Na MAS NMR of NaNbO<sub>3</sub>. *Solid State Nucl. Magn. Reson.* **2011**, *40*, 45–50.
- (34) Petříček, V.; Dušek, M.; Palatinus, L. Crystallographic computing system JANA2006: general features. *Z. Kristallogr.* **2014**, *229*, 345–352.
- (35) van Smaalen, S.; Palatinus, L.; Schneider, M. The maximum-entropy method in superspace. *Acta Crystallogr., Sect. A: Found. Crystallogr.* **2003**, *59*, 459–469.
- (36) Momma, K.; Izumi, F. VESTA 3 for three-dimensional visualization of crystal, volumetric and morphology data. *J. Appl. Crystallogr.* **2011**, *44*, 1272–1276.
- (37) Abramov, Y. A.; Tsirelson, V.; Zavodnik, V.; Ivanov, S.; Brown, I. The chemical bond and atomic displacements in SrTiO<sub>3</sub> from X-ray diffraction analysis. *Acta Crystallogr., Sect. B: Struct. Sci.* **1995**, *51*, 942–951.
- (38) Williams, R.; Dillin, D. R.; Milligan, W. Structure refinement of potassium chloroplatinate by powder and single-crystal methods. *Acta Crystallogr. Sect. B: Struct. Crystallogr. Cryst. Chem.* **1973**, *29*, 1369–1372.
- (39) Jaulmes, S.; Julien-Pouzol, M.; Laruelle, P.; Rivet, J. Variétés de haute et basse température du seleniure double de cuivre et de germanium. *Acta Crystallogr., Sect. C: Cryst. Struct. Commun.* **1991**, *47*, 1799–1803.
- (40) Onoda, M.; Ishii, M.; Pattison, P.; Shibata, K.; Yamamoto, A.; Chapuis, G. Superspace-group approach to the phase transition of Cu<sub>8</sub>GeSe<sub>6</sub>. *J. Solid State Chem.* **1999**, *146*, 355–362.
- (41) Jiang, B.; Qiu, P.; Eikeland, E.; Chen, H.; Song, Q.; Ren, D.; Zhang, T.; Yang, J.; Iversen, B. B.; Shi, X.; Chen, L. Cu<sub>8</sub>GeSe<sub>6</sub>-based thermoelectric materials with an argyrodite structure. *J. Mater. Chem. C* **2017**, *5*, 943–952.
- (42) Jabłońska, M.; Pfitzner, A. Preparation and crystal structure of (AgI)<sub>2</sub>Ag<sub>3</sub>PS<sub>4</sub>. *Z. Anorg. Allg. Chem.* **2004**, *630*, No. 1731.
- (43) Hofmann, R.; Hoppe, R. Ein neues Oxogermanat: Li<sub>8</sub>GeO<sub>6</sub> = Li<sub>8</sub>O<sub>2</sub> [GeO<sub>4</sub>]. (Mit einer Bemerkung über Li<sub>8</sub>SiO<sub>6</sub> und Li<sub>4</sub>GeO<sub>4</sub>). *Z. Anorg. Allg. Chem.* **1987**, *555*, 118–128.
- (44) Gäbler, F.; Niewa, R. Stacking Design of Inverse Perovskites: The Systems (Sr<sub>3-x</sub>Ba<sub>x</sub>N) E, E = Bi, Sb. *Inorg. Chem.* **2007**, *46*, 859–865.
- (45) Shannon, R. D. Revised effective ionic radii and systematic studies of interatomic distances in halides and chalcogenides. *Acta*

*Crystallogr., Sect. A: Cryst. Phys., Diffr., Theor. Gen. Crystallogr.* **1976**, *32*, 751–767.

(46) Potoff, A. D.; Chamberland, B. L.; Katz, L. A single crystal study of eight-layer barium managanese oxide,  $\text{BaMnO}_3$ . *J. Solid State Chem.* **1973**, *8*, 234–237.

(47) Monroe, C.; Newman, J. The impact of elastic deformation on deposition kinetics at lithium/polymer interfaces. *J. Electrochem. Soc.* **2005**, *152*, A396.

(48) Kim, K. J.; Balaish, M.; Wadaguchi, M.; Kong, L.; Rupp, J. L. M. Solid-State Li–Metal Batteries: Challenges and Horizons of Oxide and Sulfide Solid Electrolytes and Their Interfaces. *Adv. Energy Mater.* **2021**, *11*, No. 2002689.

(49) Tranqui, D.; Shannon, R.; Chen, H.-Y.; Iijima, S.; Baur, W. Crystal structure of ordered  $\text{Li}_4\text{SiO}_4$ . *Acta Crystallogr., Sect. B: Struct. Crystallogr. Cryst. Chem.* **1979**, *35*, 2479–2487.

(50) Partik, M.; Schneider, M.; Lutz, H. Kristallstrukturen von  $\text{MgCr}_2\text{O}_4$ -Typ  $\text{Li}_2\text{VCl}_4$  und Spinell-Typ  $\text{Li}_2\text{MgCl}_4$  und  $\text{Li}_2\text{CdCl}_4$ . *Z. Anorg. Allg. Chem.* **1994**, *620*, 791–795.

(51) Schippers, A.; Brandwijk, V.; Gorter, E. Derivation and discussion of crystal structures of compounds  $\text{ABX}_3$  and  $\text{A}_2\text{BX}_6$ : Part I. Derivation of the structures. *J. Solid State Chem.* **1973**, *6*, 479–492.

(52) Nilges, T.; Pfitzner, A. A structural differentiation of quaternary copper argyrodites: Structure–property relations of high temperature ion conductors. *Z. Kristallogr.* **2005**, *281*–294.

(53) Albert, S.; Pillet, S.; Lecomte, C.; Pradel, A.; Ribes, M. Disorder in  $\text{Ag}_7\text{GeSe}_5\text{I}$ , a superionic conductor: temperature-dependent anharmonic structural study. *Acta Crystallogr., Sect. B: Struct. Sci.* **2008**, *64*, 1–11.

(54) Adeli, P.; Bazak, J. D.; Park, K. H.; Kochetkov, I.; Huq, A.; Goward, G. R.; Nazar, L. F. Boosting solid-state diffusivity and conductivity in lithium superionic argyrodites by halide substitution. *Angew. Chem., Int. Ed.* **2019**, *58*, 8681–8686.